

SunnyParking: Multi-Shot Trajectory Generation and Motion State Awareness for Human-like Parking

Jishu Miao, Han Chen, Jiankun Zhai, Qi Liu, Tsubasa Hirakawa, Takayoshi Yamashita, Hironobu Fujiyoshi

Abstract—Autonomous parking fundamentally differs from on-road driving due to its frequent direction changes and complex maneuvering requirements. However, existing End-to-End (E2E) planning methods often simplify the parking task into a geometric path regression problem, neglecting explicit modeling of the vehicle’s kinematic state. This “dimensionality deficiency” easily leads to physically infeasible trajectories and deviates from real human driving behavior, particularly at critical gear-shift points in multi-shot parking scenarios. In this paper, we propose SunnyParking, a novel dual-branch E2E architecture that achieves motion state awareness by jointly predicting spatial trajectories and discrete motion state sequences (e.g., forward/reverse). Additionally, we introduce a Fourier feature-based representation of target parking slots to overcome the resolution limitations of traditional bird’s-eye view (BEV) approaches, enabling high-precision target interactions. Experimental results demonstrate that our framework generates more robust and human-like trajectories in complex multi-shot parking scenarios, while significantly improving gear-shift point localization accuracy compared to state-of-the-art methods. We open-source a new parking dataset of the CARLA simulator, specifically designed to evaluate full prediction capabilities under complex maneuvers.

Index Terms—Data-based approaches, Autonomous driving, Automated parking, End-to-End.

I. INTRODUCTION

IN the field of autonomous driving, driving and parking functions complement each other to form a complete, advanced user experience. Since its market launch, Automated Parking Assist (APA) has undergone continuous technological evolution, gradually upgrading into a fundamental function that supports high-level features such as Valet Parking Assist (VPA) and Automated Valet Parking (AVP). Its performance dictates the final quality of the parking task.

Unlike on-road driving, which is predominantly forward-moving, the automated parking task is essentially distinct. It typically involves multiple gear shifts (i.e., forward-reverse maneuvers), requests larger front-wheel steering angles, and operates with closer proximity to surrounding obstacles, leading to a higher risk of collision. Concurrently, the vehicle experiences more frequent acceleration and deceleration.

Although traditional planning methods like Hybrid A* [1] still dominate mass production solutions, their practical application is often hindered by a heavy reliance on complex

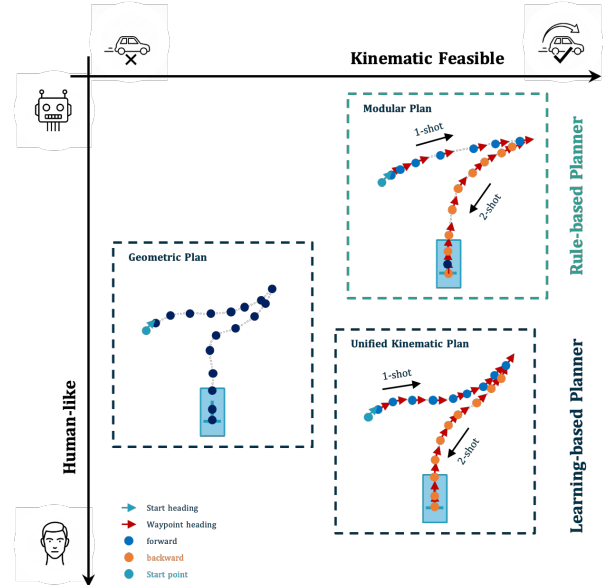


Fig. 1: Comparison of parking planning paradigms. Geometric Plan represents many current E2E approaches by focusing primarily on geometric features. Modular Plan represents the traditional rule-based paradigm (e.g., Hybrid A*). While it generates a kinematic feasible plan, achieving human-like planning remains a challenge. Our Unified Kinematic Plan achieves comparable feasibility through explicit kinematic modeling, while demonstrating superior “Human-like” qualities via its learning-based approach.

calibration and their inherent difficulty in achieving human-like driving behavior. Modern E2E learning-based approaches have become a research hotspot, showing great promise in handling complex sensor fusion and temporal prediction [2] [3] [4] [5].

However, trajectory planning studies, especially in forward-driving tasks, have primarily focused on improving the spatial accuracy of the predicted trajectory, with the core objective being the output of precise 2D coordinate waypoints. When this paradigm is directly applied to the complex, spatially-constrained environment of automated parking, its limitations are exposed. The parking task is not only a simple path-planning problem but also a complex maneuvering problem. An executable and safe parking trajectory, in addition to precise (x, y) positions, must simultaneously satisfy two other

arXiv:2602.21682v1 [cs.RO] 25 Feb 2026

Jishu Miao, Tsubasa Hirakawa, Takayoshi Yamashita, Hironobu Fujiyoshi are with Chubu University, Kasugai, Japan.

Han Chen is with Tongji University, Shanghai, China.

Jiankun Zhai, Qi Liu are independent researchers.

Manuscript received April 19, 2005; revised August 26, 2015.

dimensional constraints: an accurate heading θ and the correct corresponding motion state (i.e., forward, reverse, or stationary).

An existing gap in current E2E parking models is the lack of explicit modeling of the vehicle’s kinematic state. As shown in Fig. 1, the “Geometric Plan” approach involves training a model to fit a geometric curve but does not understand the intrinsic physical commands required to drive the vehicle along this curve. This leads to a severe deficiency in its ability to predict practically feasible trajectories. Arguably, for user acceptance, the alignment of these gear-shift points with human driver expectations can be more critical than the trajectory’s overall geometric fidelity to the ground truth. This weakness is most obvious at these critical points, where it often generates unclear or physically infeasible trajectories.

Compared to the abundance of E2E general driving datasets (e.g., NuPlan [6], Waymo Open Dataset [7], Argoverse [8] [9]), dedicated parking datasets are significantly more limited, with the majority focusing on BEV images or perception labels (e.g., CNRPark+EXT [10], DLP [11]).

To fill the aforementioned research gap, we aim to elevate parking planning from a mere geometric path regression problem to a comprehensive prediction problem of both trajectory and motion states. Experimental results demonstrate that our method achieves a 69.6% error reduction in trajectory planning. Compared to the state-of-the-art (SOTA) approaches, it not only enhances overall trajectory performance but also improves the positional accuracy of gear-shift points. Furthermore, our approach maintains robustness even in complex scenarios requiring multiple gear shifts.

To summarize, our contributions are as follows:

- We propose SunnyParking, a novel dual-branch architecture for the joint prediction of spatial trajectory and motion state. Our architecture can simultaneously output a high-precision spatial trajectory and a strictly aligned sequence of discrete motion states.
- We design a cross-domain target fusion mechanism that represents the target slot using Fourier feature mapping. This approach is not constrained by the fixed BEV resolution or performance degradation at the grid’s edges, overcoming a key limitation of traditional BEV-based schemes.
- We construct and open-source a CARLA [12] dataset containing multi-shot parking maneuvers. The dataset features parking demonstrations by expert drivers, supplying all required RGB camera and chassis data for E2E approaches.

II. RELATED WORKS

Focusing on automated parking, we organize this section into two primary parts: target point representation and trajectory planner paradigms.

A. Target Representation in Goal-Conditioned Planning

As a quintessential goal-conditioned planning task, the representation of the target parking slot critically influences performance.

1) *Goal-state Representation*: The most straightforward approach is to represent the goal as a sparse vector of its state. MPNet’s [13] Pnet explicitly uses the goal state (x, y, θ) as an input for a bidirectional path generation heuristic. It simultaneously extends a path from the start towards the goal and a second path from the goal towards the start, driving the two trajectories to converge until they can be connected.

2) *BEV Pseudo-image Representation*: To provide richer spatial priors, many studies have drawn inspiration from concepts in BEV perception [14] [15] [16] [17] [18].

E2E Parking [19] represents the target slot as a binary pseudo-image within the vehicle-centric BEV space. This is achieved by first transforming the target slot’s coordinates and then setting the hard target heatmap that forms a fixed-size square at that location. TransParking [20] further refines this approach with a gaussian kernel distribution representation. This method generates a soft target heatmap. This direct alignment allows the target features to be fused with the sensor features via element-wise addition (i.e., one-domain fusion).

However, the performance ceiling of BEV-based method is constrained by the BEV grid resolution and the downstream modules unaware of its actual heading.

3) *Fourier Feature Representation*: To overcome these drawbacks, Tancik et al., [21] mapped low-dimensional coordinates into a higher-dimensional space using sinusoidal bases. This approach allows a simple MLP to learn high-frequency details, a phenomenon known as overcoming “spectral bias” [22]. Equation (1) defines the function $\gamma(\mathbf{v})$, which maps an input low-dimensional coordinate vector \mathbf{v} to a higher-dimensional feature vector.

$$\gamma(\mathbf{v}) = \begin{bmatrix} \cos(2\pi\mathbf{B}\mathbf{v}) \\ \sin(2\pi\mathbf{B}\mathbf{v}) \end{bmatrix}. \quad (1)$$

In this mapping, the product $\mathbf{B}\mathbf{v}$ projects the input coordinate vector \mathbf{v} onto a set of random frequency directions defined by the rows of the matrix \mathbf{B} .

A key advantage of this technique is that it preserves the high-precision location of the target, bypassing the quantization errors associated with fixed grid resolutions. We adopt this representation to ensure our planner is conditioned on precise, high-fidelity goal information.

B. End-to-End Planner Paradigms

The E2E approach learns a direct mapping from sensor inputs to parking maneuvers, which typically falls into two categories: direct control or trajectory prediction.

1) *Control-based planning paradigm*: Pioneering work like PilotNet [23] [24] [19] bypass the need for a separate controller by outputting steering and throttle commands directly. However, this reactive approach is unsuitable for the deliberate, multi-step nature of parking, as its short planning horizon amplifies control errors, often leading to hesitation or deadlocks.

2) *Trajectory-based planning paradigm*: Chitta et al., [25] employ a recurrent architecture for driving trajectory generation. The fused spatial context vector subsequently initializes the hidden state of a GRU decoder [26], which then predicts the future trajectory as an ordered sequence of waypoints in

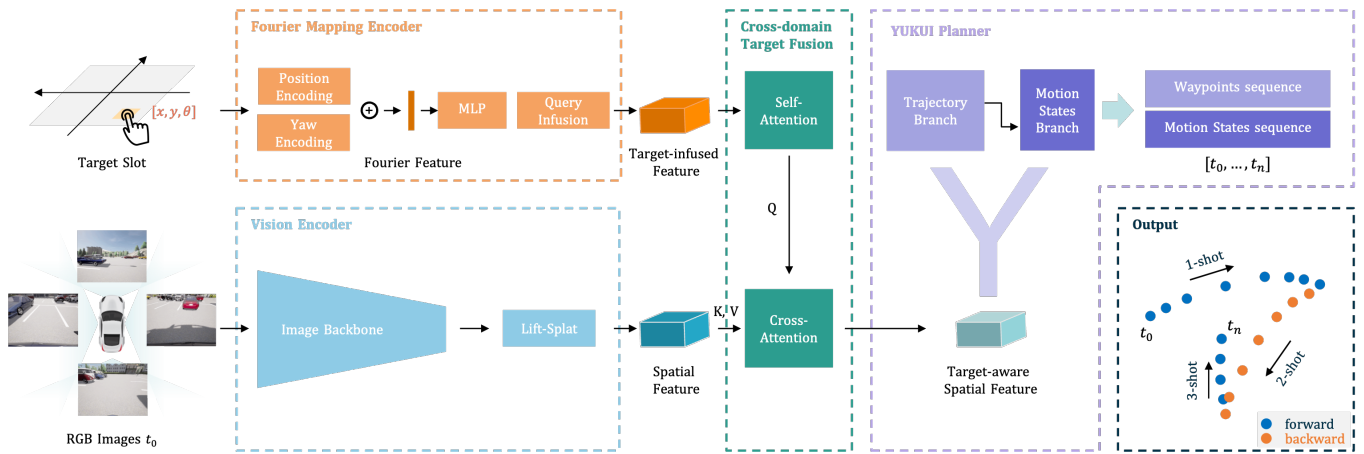


Fig. 2: **The Overview of SunnyParking’s Network Architecture.** It takes 4 RGB images as the sensory input, along side it is the selected target slot. Vision Encoder extracts the vision-domain features then project them to the BEV space as the spatial features. Fourier Mapping Encoder first represents the target including it’s (x, y, θ) in Fourier feature, then query the spatial features. In YUKUI module: Trajectory Branch takes the fused features then predicts a set of waypoints. With the additional input from Trajectory Branch’s hidden layer, Motion State Branch predicts the motion state, corresponding with each points

autoregressive manner. UniAD [27] leverages Transformer-based backbones, have demonstrated impressive performance by a simple attention-based planner in generating smooth, collision-free paths.

For the parking task, ParkingE2E [28] also cleverly leverages the autoregressive manner, employing a Transformer decoder [29] to predict the (x, y) coordinates of waypoints for N timesteps starting from the current time t_0 , at a fixed time interval. This study was validated on a real vehicle, and the experimental results demonstrated its ability to generate a solid, single-shot parking trajectory in real-world scenarios. ParkDiffusion [30] introduces diffusion models to the automated parking, generating multi-modal trajectory predictions based on perception results as input. This approach is shown to improve parking success rates and reduce collisions in complex scenarios.

These studies are primarily based on the Imitation Learning (IL) paradigm. Models relying purely on IL suffer from two main defects in trajectory prediction: distributional shift and limited generalization. To address these limitations, a clear trend in complex driving tasks is to combine Imitation Learning (as a cold start) with Reinforcement Learning (RL), [31] [32] to further optimize the final trajectory.

Nevertheless, the parking task is characterized by low speeds, high precision, and the primary objective of collision avoidance. Under these constraints, the capability of Imitation Learning to clone expert trajectories is largely sufficient for the task requirements. Therefore, the planner design in this study will continue to be based on the Imitation Learning paradigm.

III. METHODOLOGY

We introduce our proposed method, SunnyParking. This name is aptly chosen as the parking dataset used in our experiments was collected primarily under sunny, midday conditions. In this section, we will introduce the problem definition, the architecture of each module, and the design of the loss functions.

A. Preliminaries: Problem Definition

We formulate the task of imitating expert driving trajectories as a supervised learning problem. The core idea is to train a neural network to map sensor inputs to future vehicle trajectories based on expert behaviors.

Our dataset consists of M expert-driven trajectories. Each trajectory i is a time-ordered sequence of states with a total length of N_i . For any given time step j within trajectory i , the available data include:

$$\mathcal{D} = \{(I_{i,j}^k, T_{i,j}, M_{i,j}, S_i)\}, \quad (2)$$

where trajectory index $i \in [1, M]$, trajectory points index $j \in [1, N_i]$, camera index $k \in [1, R]$, RGB image I , parking trajectory waypoint T , parking motion states M , target parking slot position S .

From the raw dataset, we reorganize the dataset \mathcal{D}' . Each sample in \mathcal{D}' consists of an input pair $(I_{i,j}^k, S_i)$ and a corresponding target output pair $(T'_{i,j}, M'_{i,j})$. The targets represent the ground truth future sequences of length Q :

$$\mathcal{D}' = \{(I_{i,j}^k, T'_{i,j}, M'_{i,j}, S_i)\}. \quad (3)$$

The sequence of the trajectory waypoints $T'_{i,j}$ from the expert path and the sequence of the motion states $M'_{i,j}$:

$$T'_{i,j} = \{P_{i, \min(j+b, N_i)}\}_{b=1}^Q, \quad (4)$$

$$M'_{i,j} = \{M_{i, \min(j+b, N_i)}\}_{b=1}^Q. \quad (5)$$

To obtain motion-state labels, we extract the vehicle’s longitudinal speed from the chassis signals. A motion state is defined as:

- Forward: $v > 0.05$ m/s
- Reverse: $v < -0.05$ m/s
- Stationary: $|v| \leq 0.05$ m/s

During data preprocessing, transient states caused by neutral gear transitions are removed, and the stationary state is reserved as meaningful pauses between maneuvers. This explicit

definition ensures consistent alignment between the trajectory curvature and its corresponding motion primitives, particularly at gear-shift boundaries.

The network N_θ takes the current images and goal as input and outputs predictions for the future trajectory and motion states, structured to match the ground truth targets.

$$N_\theta(I, S) = (\hat{T}', \hat{M}'), \quad (6)$$

where \hat{T}' is the predicted waypoint sequence and \hat{M}' is the predicted motion state sequence.

The network's parameters θ are optimized by minimizing a composite loss function, \mathcal{L}_{total} , which measures the discrepancy between the predictions (\hat{T}', \hat{M}') and the ground truth targets (T', M') :

$$\theta' = \arg \min_{\theta} \mathbb{E}_{(I, T', M', S) \sim \mathcal{D}'} [\mathcal{L}((T', M'), N_\theta(I, S))], \quad (7)$$

where \mathcal{L} denotes the loss function.

B. Fourier Mapping Encoder

The key information of the target slot S_i is their position $\mathbf{p} \in \mathbb{R}^2$, $p_i = (x_i, y_i)$ and heading θ . It defines the goal position and orientation of the vehicle when it completes the parking task.

In prior work, the target slot is rasterized into a BEV grid of fixed resolution (typically 0.1–0.2 m per pixel). This inherently limits positional precision and introduces quantization artifacts near slot boundaries. As shown in our attention analysis (Fig. 6), BEV-based encoders often fail to maintain consistent localization as the slot moves across pixel boundaries, leading to periodic distortions in the planner's spatial reasoning.

Motivated by this limitation, we adopt a continuous Fourier feature mapping that preserves sub-centimeter accuracy independent of BEV grid resolution. This representation allows the target slot to condition the planner with high-frequency location cues, enabling more reliable attention modulation during multi-shot maneuvers. As shown in Fig. 2 the Fourier Mapping Encoder maps both target slot's position and heading to a high-dimensional feature vector $S_{i_encoded}$.

1) *Position Encoding*: First, we normalize the position $\mathbf{p} = (c_x, c_y)$ to the range $[-\pi, \pi]$:

$$p' = (x', y') = \frac{\pi}{C_{max}} \cdot p, \quad (8)$$

resulting in $\mathbf{p}' = (x', y')$, where C_{max} is the range of the actual area of the BEV spatial feature will be represented. Then, it applies the encoding function $\gamma(v)$ as below:

$$\begin{aligned} \gamma_{pos}(p') = & [\sin(2^0 p'), \cos(2^0 p'), \sin(2^1 p'), \cos(2^1 p'), \\ & \dots, \sin(2^{L-1} p'), \cos(2^{L-1} p')], \end{aligned} \quad (9)$$

where L is the number of frequencies.

As the (10) shows the final position encoding is a concatenation of \mathbf{p}' and its Fourier features.

$$\mathcal{F}_{pos} = [x', y', \gamma_{pos}(x'), \gamma_{pos}(y')]. \quad (10)$$

By setting the parameter $L = 12$, the theoretical resolution is around 1.2 cm, the practical effective precision of our method reaches 1 – 2 mm. This achieved precision is finer-grained than the BEV grid's representational capacity.

2) *Yaw Encoding*: To handle the heading angle θ of the target slots, the heading is mapped to a 2D vector, as shown below:

$$\mathcal{F}_{yaw} = [\sin(\theta), \cos(\theta)]. \quad (11)$$

For the final output of the target encoder, Fourier encoded target \mathbf{t}_{enc} is obtained by concatenating positional and yaw features: $\mathbf{t}_{enc} = [\mathcal{F}_{pos}, \mathcal{F}_{yaw}]$.

C. Cross-domain Target Fusion

To leverage the precise position and heading information provided by the Fourier encoded target \mathbf{t}_{enc} , it is fused with the BEV feature map \mathcal{F}_{BEV} efficiently. Different from the conventional methods that fuse the two BEV-based feature maps directly, we designed a Cross-domain Target Fusion module. It utilizes the Fourier encoded target to modulate a set of learnable spatial queries, and then uses these target-aware queries to extract the relevant information from the BEV feature map. These queries dynamically constructed from two sources of information.

1) *Target projection*: an MLP module is applied for projecting the low-dimensional \mathbf{t}_{enc} to a high-dimensional channel C , the same as the channel of the BEV feature map to create a shared global target vector \mathbf{t}_{global} .

2) *Query Infusion*: a set of learnable spatial query tokens $\{\mathbf{s}_j\}_{j=1}^N$, where $N = H \times W$ matches the shape of the BEV feature map. This set learns the prior information for each of the N locations. The infusion is accomplished via element-wise addition:

$$\mathbf{q}_j = \mathbf{s}_j + \mathbf{t}_{global}. \quad (12)$$

Thus, the target-infused query \mathbf{q}_j encodes both its spatial prior and the shared global context.

3) *Target-Spatial Information Fusion*: Flattening the BEV feature map F_{BEV} and giving it a positional embedding, we then treat it as the Key and Value, and the target-infused query \mathbf{q}_j as Query to the transformer decoder. Then it outputs the target-aware, context-enriched features $\mathcal{F}_{enchanced}$ for their corresponding spatial locations.

D. YUKUI Planner

The philosophy of our neural planner is to predict the trajectory while considering the vehicle kinematic of each waypoint. As shown in Fig. 2, the combination of the trajectory branch and motion state branch resembled a Y-shaped Unified Kinematic and Uncertainty-aware Imitation planner, so we call it YUKUI.

1) *Goal Serialization*: The goal of YUKUI is to determine the trajectory and the motion state. By serializing the goal (i.e., waypoints and motion states), the prediction task is converted into a token prediction problem.

The serialization method for trajectories is utilized as follows:

$$\text{Ser}(P_{i,j}^k) = \left\lfloor \frac{|P_{i,j}^k + R_k|}{2R_k} \right\rfloor \times N_u, \quad \text{where } k \in \{x, y, \theta\} \quad (13)$$

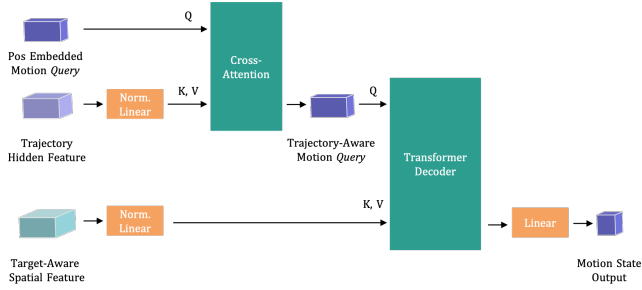


Fig. 3: **The Architecture of Motion State Branch.** Motion Query is enriched by the trajectory feature via cross-attention. This resulting the fused Queries is then input to a Transformer Decoder.

where N_u is the maximum value that a trajectory token can encode in a sequence. $\text{Ser}(\cdot)$ is the serialized waypoints. R_x, R_y, R_θ represent the maximum values of the predicted range in direction (x, y) , and the heading θ .

Although the dataset includes a stationary state, we serialize only the forward and backward components for two reasons: (1) stationary intervals do not require directional reasoning and can be inferred from near-zero speed during deployment, and (2) our preliminary experiments showed that including a third token increased label imbalance and degraded shift-point localization. Thus, the model predicts two “directional” primitives (forward, backward), while stationary periods are handled implicitly via the smoothness loss described in Sec. III-E.

The serialization method for the motion state is utilized as follows:

$$\text{Ser}(M_{i,j}^k) = [M_{i,j}^m] \times N_v, \quad \text{where } m \in \{\text{fwd}, \text{bwd}\}. \quad (14)$$

Here, N_v is the maximum value that a motion token can encode in a sequence. $\text{Ser}(\cdot)$ is the serializing motion states. $M_{i,j}^{\text{fwd}}$ and $M_{i,j}^{\text{bwd}}$ represent the serialized probabilities of *go forward* and *go backward*.

Both sequences share the same temporal length of N_i steps and maintain a one-to-one correspondence at each time step. The complete sequence formulations are as follows:

$$\begin{aligned} S_{i,\text{traj}}^k &= [BOS, \text{Ser}(P_{i,1}^k), \dots, \text{Ser}(P_{i,N_i}^k), EOS], \\ S_{i,\text{motion}}^m &= [BOS, \text{Ser}(M_{i,1}^m), \dots, \text{Ser}(M_{i,N_i}^m), EOS]. \end{aligned} \quad (15)$$

2) *Trajectory Branch*: We introduce a Transformer decoder for predicting waypoints. The target-aware features $\mathcal{F}_{\text{enhanced}}$ serve as the Key and Value, while a set of N learnable queries serve as the Query input.

3) *Motion State Branch*: To predict the vehicle motion state, as shown in Fig. 3, a key design is two-stage query-fusion mechanism. First, the Motion Query embeddings are refined by attending to the hidden layer features from the trajectory branch. In this way, the fused query is already contextually aware of the trajectory features. Then, a lighter Transformer Decoder uses the target-aware features $\mathcal{F}_{\text{enhanced}}$ as Key and Value. This allows the trajectory-aware motion query to efficiently extract the relevant spatial and contextual information from the BEV features.

E. Loss Function

The network’s parameters θ are optimized by minimizing a composite loss function $\mathcal{L}_{\text{total}}$, which measures the discrepancy between the predictions (\hat{T}, \hat{M}') and the ground truth targets (T, M') . The total loss is a weighted sum of two component losses:

$$\mathcal{L}_{\text{total}} = \lambda_{\text{waypoints}} \mathcal{L}_{\text{waypoints}} + \lambda_{\text{motion}} \mathcal{L}_{\text{motion}}. \quad (16)$$

The waypoint loss $\mathcal{L}_{\text{waypoints}}$ is the mean squared error (MSE) between T and \hat{T} . As (17) shows, the motion loss $\mathcal{L}_{\text{motion}}$ is combined with a Mean Cross-Entropy (MCE) loss λ_{CE} between the probability distributions in \hat{M}' and the one-hot labels in M' , and a GT-awareness smoothness loss λ_{smooth} .

$$\mathcal{L}_{\text{motion}} = \mathcal{L}_{\text{CE}} + \lambda_{\text{smooth}} \mathcal{L}_{\text{smooth}}. \quad (17)$$

To reduce the motion state shaking in hesitant areas, we designed a GT-awareness smoothness loss avoid to penalize the network for predicting correct, clear gear-shift points. It is implemented as a masked L1 loss but applies a mask that deactivates the loss calculation with a tolerance window surrounding the ground truth gear-shift locations, enforcing smoothness only in stable and non-shifting regions.

IV. EXPERIMENTS

A. Training Configuration and Optimization

Following the data acquisition pipeline of E2E Parking [19], we collected our parking dataset based on CARLA Simulator (Detailed description is in Appendix A).

We train our model for a total of 30 epochs using a batch size of 24, distributed across 2 RTX A6000 GPUs. We use the Adam optimizer with an initial learning rate of 2×10^{-4} . A cosine annealing learning rate schedule is employed, which includes warmup and decays the learning rate from 2×10^{-4} to 1×10^{-6} . To ensure training stability, we apply gradient clipping with a threshold of 0.5. Mixed precision training (FP16) is enabled to accelerate computation. We set the 2D area within the VCS, and let a BEV field of view (FOV) of real area at a size of $[-10, 10]$ m of x, y axis, and the BEV feature map of 200×200 . Thus the resolution of 0.1 m/pixel. During training, we add uniform noise of ± 0.3 m to the target position (x, y) and $\pm 2.0^\circ$ to the target yaw θ . In trajectory decoder, the maximum value of N_u is 1200, and in motion

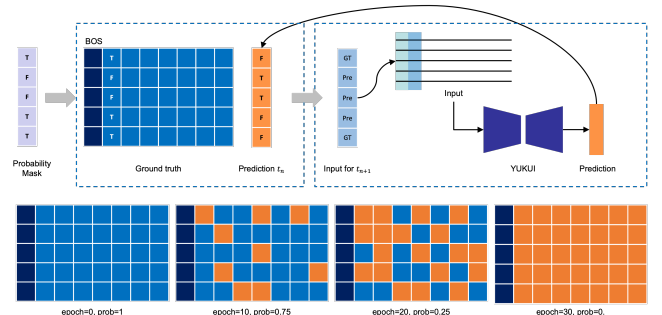


Fig. 4: Progressive transition from teacher forcing to autoregressive prediction via Scheduled Sampling.

TABLE I: Performance Evaluation of Trajectory and Gear Shift Points.

Methods	Waypoints Error				Gear Shift Points Error				
	L2 Dis.	Four. Diff.	Haus. Dis.	AHE	2S[P_1]	3S[$P_1 - P_2$]	4S[$P_1 - P_2 - P_3$]	Avg.	
TransFuser [25]*	1.077	19.949	1.154	/	1.528	/ - /	/ - / - /	1.528	
ParkingE2E [28]	3.505	40.032	3.760	/	5.28	6.578 - 2.509	2.679 - / - /	5.685	
Ours	1.065	19.282	1.169	5.5	1.211	0.974 - 1.077	1.083 - 1.064 - 0.817	1.152	

* **Note:** Indicates a modified TransFuser adapted to a vision-only setting using same Vision Encoder with 4 surround-view images, and the Goal Location is set as the target slot's 2D coordinates.

TABLE II: Ablation Study of Different Model Components.

Set	Input Rep.		Model Comp.		Sched. Sampling	Trajectory Metrics				Motion State Metrics	
	BEV	Fourier	Traj.	Motion		L2 Dis.	Four. Diff.	Haus. Dis.	AHE	Acc.	Avg. Dist.
1	✓		✓			3.505	40.033	3.760	/	/	/
2	✓		✓		✓	2.327	39.492	2.408	/	/	/
3	✓		✓ _{ext}	✓		1.474	27.253	1.635	9.8	0.827	1.900
4	✓		✓ _{ext}	✓	✓	1.800	37.253	2.160	11.7	0.794	2.385
5		✓	✓			2.863	55.885	3.172	/	/	/
6		✓	✓		✓	2.680	44.539	3.071	/	/	/
7		✓	✓ _{ext}	✓		1.065	19.282	1.169	5.5	0.838	1.152
8		✓	✓ _{ext}	✓	✓	1.421	24.490	1.714	7.3	0.758	1.531

state decoder, the maximum value of N_v is 100. Both decoders generate a sequence of predictions with a length of 30. To ensure fair comparison, we utilize the official implementations and widely-adopted hyperparameters for the baseline method.

For exposure bias problem, we employ a scheduled sampling strategy to bridge the exposure bias between training (teacher forcing) and validation/inference (autoregressive). As shown in Fig. 4, this strategy starts at epoch 5 and concludes at epoch 25. During this period, the probability of feeding the ground-truth token to the next time step linearly decays from 1.0 down to 0.0. After epoch 25, the model continues training in a fully autoregressive mode.

The total loss \mathcal{L}_{total} is a weighted sum of the trajectory prediction loss and the motion state prediction loss, we use fixed weights for $\mathcal{L}_{waypoints}$, \mathcal{L}_{motion} , and \mathcal{L}_{smooth} . During the loss calculation, all padding (PAD) tokens are ignored.

B. Evaluation Metrics

We focus on both the trajectory and motion state prediction performance of the YUKUI.

1) *Trajectory Evaluation:* By calculating the error between the predicted trajectory and the ground truth, we evaluate the multi-shot parking trajectory using the following metrics: L2 Distance error (L2 Dis.), Fourier descriptor distance error (Four. Diff.), and Hausdorff distance error (Haus. Dis.). Additionally, Average Heading Error (AHE) is calculated by taking the mean of the absolute angular differences between the predicted and ground-truth at each corresponding waypoint.

2) *Motion State Evaluation:* As we predict the motion state of each waypoint, two vital information are obtained: the general vehicle kinematic state and the trajectory shape change points (i.e., gear-shift positions).

We classify a parking trajectory according to the number of gear-shift operations observed in the ground truth demonstration:

- 1-shot: 0 gear shifts
- 2-shot: 1 gear shift
- 3-shot: 2 gear shifts
- 4-shot: 3 gear shifts

A gear-shift point is defined as the timestamp at which the motion state transitions between {forward \rightarrow reverse} or {reverse \rightarrow forward}. Stationary intervals without a directional change are not counted as gear shifts. This classification enables a structured analysis of increasingly complex parking behaviors.

Motion State Accuracy is defined as the percentage of timesteps which the dominant motion state (i.e., the state with the higher probability) is correctly predicted. We compute the predicted motion state $\hat{c}_{i,j}$ and the ground-truth motion state $c_{i,j}$ at each step:

$$\hat{c}_{i,j} = \arg \max_{m \in \{\text{fwd}, \text{bwd}\}} (\hat{M}_{i,j}^m) \quad \text{and} \quad c_{i,j} = \arg \max_{m \in \{\text{fwd}, \text{bwd}\}} (M_{i,j}^m). \quad (18)$$

The accuracy is the mean of an indicator function $\mathbb{1}$ over all timesteps:

$$M_{acc} = \frac{1}{B \cdot N} \sum_{i=1}^B \sum_{j=1}^N \mathbb{1}(\hat{c}_{i,j} = c_{i,j}). \quad (19)$$

Gear-shift Point Position Error evaluates the 2D spatial accuracy of correctly predicted gear shifts. It measures the L2 distance between a ground-truth shift waypoint p and its matched prediction \hat{p} :

$$d(p, \hat{p}) = \|p - \hat{p}\|_2. \quad (20)$$

Trajectories are grouped by complexity based on the number of ground-truth gear shifts k . For each k -shot category, we first calculate the mean error for the n -th sequential shift point P_n across all samples:

$$M_{\text{shift}}(k\text{-shot}, P_n) = \frac{1}{C_{k,n}} \sum_{(p, \hat{p}) \in S_{k,n}} \|p - \hat{p}\|_2, \quad (20)$$

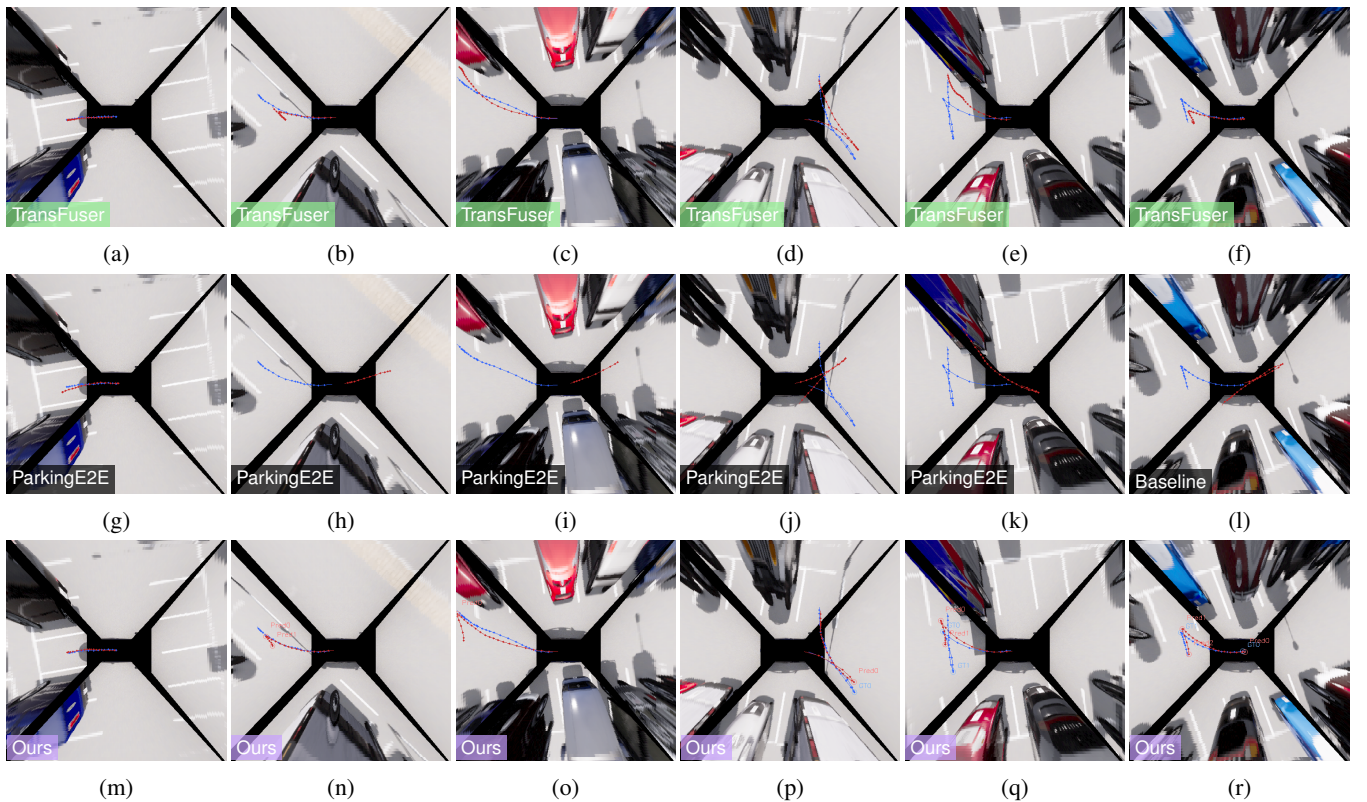


Fig. 5: **Qualitative Comparison of Parking Planning Results.** Blue represents the GT trajectory, while red indicates the prediction. As task complexity increases, baseline methods struggle: TransFuser fails to generate feasible trajectories, while ParkingE2E exhibits overfitting to specific parking patterns. Our method produces robust trajectories with correctly predicted gear shift points. Notably, as shown in (o), our method demonstrates superior feature representation capabilities. It effectively handles regions near the boundaries of the BEV FOV, comparable to the direct 2D coordinate input strategy used in TransFuser.

where $S_{k,n}$ is the set of all matched pairs for the n -th shift in this category, and $C_{k,n}$ is the total count. Finally, the category-level average error is the mean of these sequential shift errors:

$$M_{\text{avg}}(k\text{-shot}) = \frac{1}{k} \sum_{n=1}^k M_{\text{dist}}(k\text{-shot}, P_n). \quad (21)$$

C. Quantization Results

To comprehensively validate the effectiveness of the proposed method, we selected the optimal model version for evaluation and employed the representative TransFuser [25] and ParkingE2E [28] as baseline methods.

As shown in Table II, our approach achieved superior performance across most key metrics for waypoint error. Furthermore, we achieve an average heading prediction accuracy of approximately 5.488° , which is absent in the baseline.

Regarding gear-shift point error, we conduct an intensive investigation into the model’s advantages in multi-shot parking scenarios. The motion state results indicate that the performance of the conventional methods on both the accuracy of gear-shift position prediction and the success rate of predicting the actual number of gear shifts decreases significantly as task complexity (i.e., the number of gear shifts) increases. This demonstrates that conventional architecture of the single

trajectory branch possesses inherent limitations when processing trajectories of high complexity and multiple transitions in motion states. In contrast, our approach maintains accurate positioning between shift points and precisely predicts the number of shifts even within the most complex 4-shot scenarios $4S[P_1 - P_2 - P_3]$.

D. Ablation Studies

Table II presents a comprehensive ablation study to validate the contribution of each proposed component. Our trajectory branch which includes an auxiliary heading prediction is denoted as with the “*ext*” subscript in the ‘Traj.’ column (e.g., Set 3, 4, 7, 8). We designed 8 experimental sets to investigate three key variables:

- **Input Representation:** Comparing BEV features against our proposed Fourier-based embedding.
- **Model Components:** Evaluating the baseline single trajectory decoder (*Traj.*) versus our dual-branch architecture (*Traj_{ext}* + *Motion*).
- **Training Strategy:** Assessing the impact of Scheduled Sampling on different model capacities.

The most significant performance leap stems from explicitly modeling motion states. Comparing purely geometric baselines (Set 1, 5) with dual-branch models (Set 3, 7), introducing the motion decoder drastically reduces the L2 Distance error (e.g.,

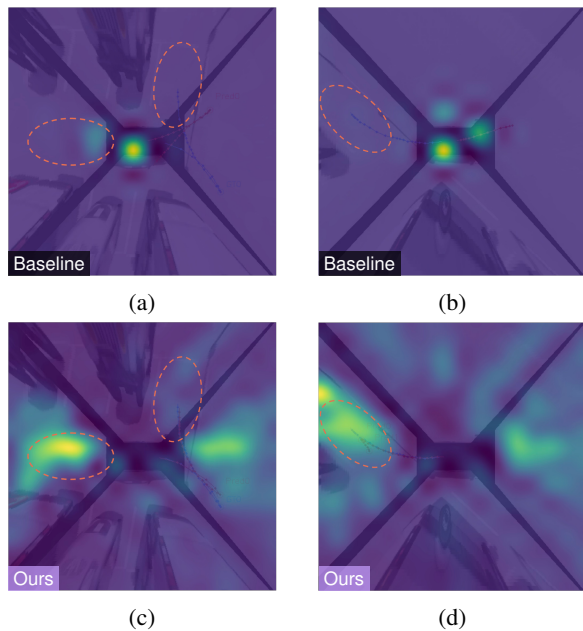


Fig. 6: **Comparison of Attention Heatmaps between Baseline (BEV) and Ours (Fourier).** Our method exhibits an attention shift as the relative position between the ego rear and the target slot changes.

from 2.863 m to 1.065 m in Fourier-based models). This confirms our hypothesis that understanding the motion state is a prerequisite for accurate complex trajectory generation.

While BEV features provide a reasonable baseline, Fourier-based representation consistently outperforms them when combined with the full model architecture. Set 7 achieves the lowest L2 Distance error of 1.065 m, surpassing the best BEV configuration (Set 3 as 1.474 m), indicating its stronger capability in capturing fine-grained trajectory details.

Scheduled Sampling exhibits a dual effect. It acts as a beneficial regularizer for simpler models (improving Set 1 to Set 2). However, for our capable full model, it tends to hinder performance (degrading Set 7 to Set 8), likely introducing unnecessary noise during the training of the highly sensitive dual-branch structure.

E. Visualization Results

We evaluate qualitative performance by visualizing trajectory outputs and gear-shift points across scenarios of varying complexity (i.e., Set 1 vs. Set 7).

As Fig. 5 shows, with the increasing complexity of scenarios, our method proves significantly more robust than the baseline methods, maintaining high accuracy in predicting gear-shift frequency and location while ensuring trajectory smoothness. In some simple scenarios (Fig. 5n, 5o), our model tends to plan 3-shot maneuvers even where human drivers (GT) achieve a 1-shot parking. This likely stems from the dataset’s long-tail distribution, which is heavily skewed towards 3-shot examples (see Appendix A-D). Furthermore, while generated trajectories are continuous and kinematically reasonable, they sometimes deviate from the GT. This reflects

an inherent limitation of open-loop imitation learning, which aims to mimic specific expert demonstrations rather than exploring the full feasible solution space. Although closed-loop testing is needed to fully validate ultimate success rates, current results sufficiently demonstrate our planner’s superiority in complex scenarios.

We visualized the attention heatmaps of the Target-Spatial fusion module to understand the mechanisms driving these gains. The significant attention degradation in the Baseline during multi-shot scenarios in Fig. 6. It frequently suffers from periodic artifacts due to position encoding errors, and in severe cases, collapses into rigid patterns decoupled from the input—essentially “memorizing” average dataset positions rather than planning based on the scene. In contrast, by explicitly modeling planning intent, our method demonstrates superior active understanding. The model proactively shifts attention to the vehicle’s rear (see Fig. 6c) and the target slot (see Fig. 6d) when predicting reverse motions. This ensures attention remains strictly aligned with the immediate planning intent throughout the long-term maneuver.

V. CONCLUSION

In this study, we propose an end-to-end dual-task parallel trajectory prediction framework. By introducing an additional motion state branch, the model significantly enhances its ability to predict the motion state transition points (e.g., gear-shift points) in multi-shot parking trajectories. We employ Fourier feature mapping to encode target point into query vectors, which interact with sensor features in the BEV to achieve cross-domain information fusion. Experimental results demonstrate that our dual-branch model not only exhibits a superior trajectory handling capability in complex parking scenarios but also sensitively captures distinct human driver parking styles. This effectively avoids the problem of previous models tending to overfit simple high-scoring trajectories (e.g., 1-shot parking). Our future work will focus on extend our study to more complex real-world scenarios, prioritizing enhancements in the model’s ability to predict interactions with dynamic traffic participants and deepen its semantic understanding of complex environments.

APPENDIX A

CARLA HUMAN-DRIVEN PARKING DATASETS DETAILS

To create a comprehensive and challenging dataset, we generate a series of parking scenarios within the Town04_Opt environment in CARLA 0.9.13 simulator. The generation process is twofold: populating the environment with static vehicles and systematically placing the ego vehicle at diverse initial poses.

A. Static Environment Generation

As shown in Fig. 7, for each of the 16 designated target slots, we populate the remaining parking spaces with static vehicles to simulate a realistic parking lot environment. The pose (x, y, ψ) of each static vehicle is randomized as follows:



Fig. 7: Data Collection Scenario of the Parking Lot in BEV. The orange boxes represent the 16 target slots, while the blue spots are the start points for a specific task \mathbf{T} (i.e., “task 11”). The ego vehicle pose is determined by (24).

- **Base Orientation** (ψ_{base}): We simulate the two most common parking patterns for the static vehicles on perpendicular slots. The base orientation is randomly set to either 0° (head-in parking) or 180° (back-in parking).
- **Yaw Jitter** (δ_ψ): A small random yaw offset is added to simulate imperfect parking, drawn from a clipped Normal distribution at range $[-8^\circ, 8^\circ]$.

The final heading of a static vehicle is $\psi_{\text{vehicle}} = \psi_{\text{base}} + \delta_\psi$.

B. Ego Vehicle Initial Pose Generation

To ensure comprehensive coverage of starting positions around each target slot, we devise a systematic generation strategy combining a deterministic grid with stochastic jitter.

The base pose ($x_{\text{base}}, y_{\text{base}}, \psi_{\text{base}}$) is positioned relative to the target slot’s entrance, ensuring the vehicle starts on the main access lane. Its yaw is set perpendicular to the lane. A deterministic 2D grid \mathcal{G} is defined to systematically sample start points covering a wide area in front of the target slot. An offset ($x_{\text{offset}}, y_{\text{offset}}$) is selected from this grid for each scenario:

$$x_{\text{offset}} \in \{-x_r, -x_r + x_s, \dots, x_r\}, \quad (22)$$

$$y_{\text{offset}} \in \{-y_r, -y_r + y_s, \dots, y_r\}, \quad (23)$$

where the range x_r , and y_r are set to $[-1, 1]$ m and $[-10, 10]$ m, respectively, with step sizes of $x_s = 1$ m, and $y_s = 2$ m. To guarantee each spawn pose is unique and to introduce fine-grained variations, a stochastic jitter term is applied to both position and orientation: $x_{\text{jitter}}, y_{\text{jitter}} \sim \mathcal{U}(-0.2, 0.2$ m, and $\psi_{\text{jitter}} \sim \mathcal{U}(-15^\circ, 15^\circ)$.

The final spawn pose is thus the sum of these components, creating a diverse yet structured distribution of initial conditions for robust model training and evaluation.

$$\begin{aligned} x_{\text{spawn}} &= x_{\text{base}} + x_{\text{offset}} + x_{\text{jitter}}, \\ y_{\text{spawn}} &= y_{\text{base}} + y_{\text{offset}} + y_{\text{jitter}}, \\ \psi_{\text{spawn}} &= \psi_{\text{base}} + \psi_{\text{jitter}}. \end{aligned} \quad (24)$$



Fig. 8: A human driver is performing a parking maneuver.

C. Data Acquisition

8 drivers performed parking maneuvers using the Logitech G29 controller to operate the steering wheel, gearbox, throttle, and braking pedals. This hardware configuration replicates the linearity of actual driving, generating smooth, continuous control signals distinct from step-wise computer peripherals.

We configured an operational steering limit of 30° to mirror the soft-limit strategy of real-world chassis controllers. This design aligns the simulation with physical engineering practices, ensuring the generated parking maneuvers faithfully replicate real-vehicle behaviors.

We set the criteria for successful parking as the Euclidean distance being less than 0.25 m and the heading angle being less than 2.5° . Multi-modal data are synchronously collected during park-in task execution at a 5 Hz frequency, specifically comprising:

- **Perception Data:** Four surround-view RGB camera images and corresponding depth maps.
- **Ego-Vehicle State:** High-precision vehicle positioning data (including position x, y and orientation ψ), alongside detailed chassis signals (e.g., speed, acceleration, throttle, brake, and gear status).
- **Task Information:** Precise position and orientation of the target parking slot.
- **Environment Data:** Category, position, orientation, and 3D bounding box information for surrounding static obstacles (e.g., other vehicles),

TABLE III: Consolidated Sensor Specifications

Sensor	Count	Resolution	FOV
RGB Camera	4	400×300 px	100°
Depth Camera	4	400×300 px	100°
IMU	1	Accelerometer (3-axis), Gyroscope (3-axis), Compass	
GNSS	1	Provides Latitude, Longitude	
Vehicle State	–	Position, Orientation, Speed, Throttle, Brake, Steer, Gearbox	

D. Data Analysis

The raw collected data contained significant redundancy and non-standard driving behaviours. To construct a focused,

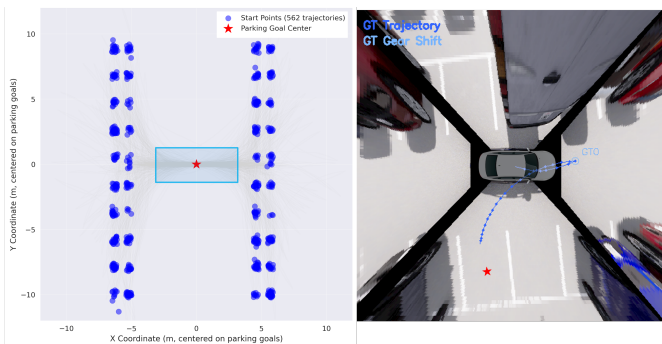


Fig. 9: Distribution Map of Parking Start Point. All target parking slots are normalized to the center of the image. It can be seen that for parking in one side, there are 20 start points (2 columns by 10 rows), accompanied by a certain amount of jitter.

efficient dataset that aligns with human drivers’ actual parking habits and intentions [33], we first concentrated the data on parking tasks involving 0 to 3 gear changes. Then we defined the *valid slice* of parking tasks: the start time is when the vehicle’s throttle first produces actual acceleration, and the end time is when the vehicle comes to a complete stop at the target parking slot with a speed of zero, while ignoring instances where the gearbox passed through neutral gear during gear changes.

Based on this valid slice, subsequent statistical analyses were conducted. All trajectory tasks were categorized by gear shift count ($N_{\text{shift}} \in \{0, 1, 2, 3\}$). Statistical analysis was performed across three dimensions: average speed, slice length, and trajectory length. The distribution across the four categories is illustrated below:

As shown in Fig. 10, the original data distribution is extensive. To avoid any extreme outliers and obtain the most representative core data, we retained only those trajectories within each category where all three dimensions fell within the [10%, 90%] range. This formed our core dataset. We consider zero gear changes (1-shot parking) to represent the smoothest and most efficient parking maneuver, serving as an ideal baseline. The specific interval thresholds applied for each category are as follows:

TABLE IV: Data Filtering Thresholds and Final Task Distribution

Category	Avg. Speed (km/h)	Slice Len. (frames)	Traj. Len. (m)	Count
1-shot		Unconstrained		25
2-shot	[2.90, 6.70]	[101, 210]	[12.8, 25.2]	111
3-shot	[2.79, 5.70]	[125, 219]	[14.0, 22.5]	120
4-shot	[2.83, 6.00]	[144, 280]	[17.0, 31.0]	306
Total				562

Following the data cleaning process detailed in Table IV, the final dataset comprises 562 parking tasks. As shown in the last column, the distribution is skewed towards complex maneuvers, with 4-shot cases accounting for the majority 54% of the dataset.

REFERENCES

- [1] D. Dolgov, S. Thrun, M. Montemerlo, and J. Diebel, “Path planning for autonomous vehicles in unknown semi-structured environments,” *The international journal of robotics research*, vol. 29, no. 5, pp. 485–501, 2010.
- [2] A. Sadat, M. Ren, A. Pokrovsky, Y.-C. Lin, E. Yumer, and R. Urtasun, “Jointly learnable behavior and trajectory planning for self-driving vehicles,” in *2019 IEEE/RSJ International Conference on Intelligent Robots and Systems (IROS)*. IEEE Press, 2019, pp. 3949–3956. [Online]. Available: <https://doi.org/10.1109/IROS40897.2019.8967615>
- [3] J. Gu, C. Sun, and H. Zhao, “Densetnet: End-to-end trajectory prediction from dense goal sets,” in *2021 IEEE/CVF International Conference on Computer Vision (ICCV)*, 2021, pp. 15283–15292.
- [4] P. Cai, Y. Sun, H. Wang, and M. Liu, “Vtgnnet: A vision-based trajectory generation network for autonomous vehicles in urban environments,” *IEEE Transactions on Intelligent Vehicles*, vol. 6, no. 3, pp. 419–429, 2021.
- [5] P. Cai, S. Wang, Y. Sun, and M. Liu, “Probabilistic end-to-end vehicle navigation in complex dynamic environments with multimodal sensor fusion,” *IEEE Robotics and Automation Letters*, vol. 5, no. 3, pp. 4218–4224, Jul. 2020.
- [6] H. Caesar, J. Kabzan, K. S. Tan, W. K. Fong, E. Wolff, A. Lang, L. Fletcher, O. Beijbom, and S. Omari, “nuPlan: A closed-loop ml-based planning benchmark for autonomous vehicles,” *arXiv preprint arXiv:2106.11810*, 2021.
- [7] S. Ettinger, S. Cheng, B. Caine, C. Liu, H. Zhao, S. Pradhan, Y. Chai, B. Sapp, C. Qi, Y. Zhou, Z. Yang, A. Chouard, P. Sun, J. Ngiam, V. Vasudevan, A. McCauley, J. Shlens, and D. Anguelov, “Large scale interactive motion forecasting for autonomous driving : The waymo open motion dataset,” in *2021 IEEE/CVF International Conference on Computer Vision (ICCV)*, 2021, pp. 9690–9699.
- [8] M.-F. Chang, J. W. Lambert, P. Sangkloy, J. Singh, S. Bak, A. Hartnett, D. Wang, P. Carr, S. Lucey, D. Ramanan, and J. Hays, “Argoverse: 3d tracking and forecasting with rich maps,” in *Conference on Computer Vision and Pattern Recognition (CVPR)*, 2019.
- [9] B. Wilson, W. Qi, T. Agarwal, J. Lambert, J. Singh, S. Khandelwal, B. Pan, R. Kumar, A. Hartnett, J. K. Pontes, D. Ramanan, P. Carr, and J. Hays, “Argoverse 2: Next generation datasets for self-driving perception and forecasting,” in *Proceedings of the Neural Information Processing Systems Track on Datasets and Benchmarks (NeurIPS Datasets and Benchmarks 2021)*, 2021.
- [10] G. Amato, F. Carrara, F. Falchi, C. Gennaro, C. Meghini, and C. Vairo, “Deep learning for decentralized parking lot occupancy detection,” *Expert Systems with Applications*, vol. 72, pp. 327–334, 2017.
- [11] X. Shen, M. Lacayo, N. Guggilla, and F. Borrelli, “Parkpredict+: Multimodal intent and motion prediction for vehicles in parking lots with cnn and transformer,” in *2022 IEEE 25th International Conference on Intelligent Transportation Systems (ITSC)*, 2022, pp. 3999–4004.
- [12] A. Dosovitskiy, G. Ros, F. Codevilla, A. Lopez, and V. Koltun, “CARLA: An open urban driving simulator,” in *Proceedings of the 1st Annual Conference on Robot Learning*, ser. Proceedings of Machine Learning Research, S. Levine, V. Vanhoucke, and K. Goldberg, Eds., vol. 78. PMLR, 13–15 Nov 2017, pp. 1–16. [Online]. Available: <https://proceedings.mlr.press/v78/dosovitskiy17a.html>
- [13] A. H. Qureshi, Y. Miao, A. Simeonov, and M. C. Yip, “Motion planning networks: Bridging the gap between learning-based and classical motion planners,” *IEEE Transactions on Robotics*, vol. 37, no. 1, pp. 48–66, 2021.
- [14] J. Philion and S. Fidler, “Lift, splat, shoot: Encoding images from arbitrary camera rigs by implicitly unprojecting to 3d,” in *Proceedings of the European Conference on Computer Vision*, 2020.
- [15] J. Huang, G. Huang, Z. Zhu, Y. Yun, and D. Du, “Bevdet: High-performance multi-camera 3d object detection in bird-eye-view,” *arXiv preprint arXiv:2112.11790*, 2021.
- [16] Z. Liu, H. Tang, A. Amini, X. Yang, H. Mao, D. Rus, and S. Han, “Bevfusion: Multi-task multi-sensor fusion with unified bird’s-eye view representation,” in *IEEE International Conference on Robotics and Automation (ICRA)*, 2023.
- [17] H. Liu, Y. Teng, T. Lu, H. Wang, and L. Wang, “Sparsebev: High-performance sparse 3d object detection from multi-camera videos,” in *2023 IEEE/CVF International Conference on Computer Vision (ICCV)*, 2023, pp. 18534–18544.
- [18] Z. Xia, Z. Lin, X. Wang, Y. Wang, Y. Xing, S. Qi, N. Dong, and M.-H. Yang, “Henet: Hybrid encoding for end-to-end multi-task 3d perception from multi-view cameras,” in *Proceedings of the European Conference on Computer Vision*, 2024.

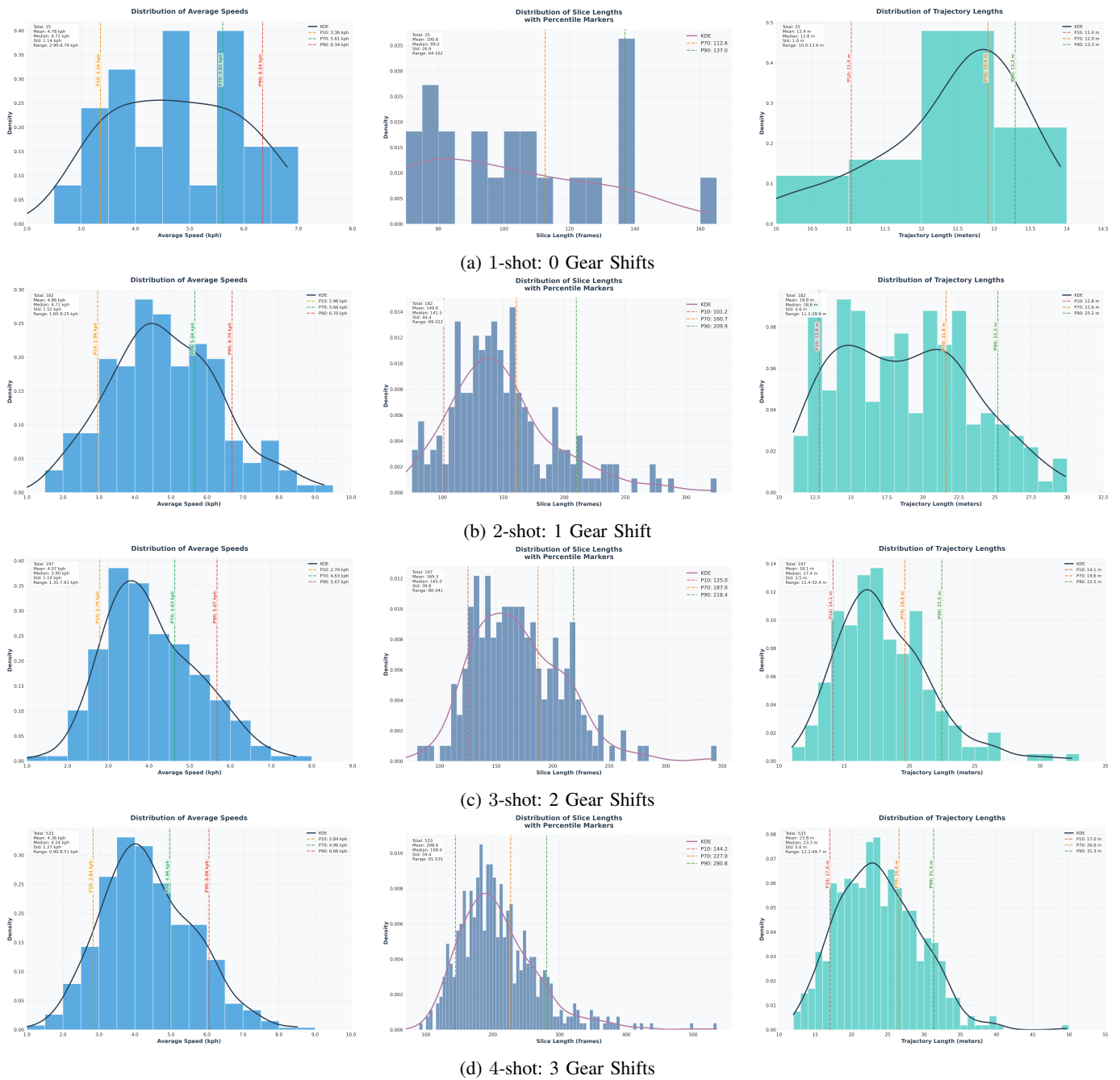


Fig. 10: Overview of data distributions for core metrics, grouped by the number of gear shifts. From left to right: Average Speed, Slice Length, and Trajectory Length.

[19] Y. Yang, D. Chen, T. Qin, X. Mu, C. Xu, and M. Yang, "E2e parking: Autonomous parking by the end-to-end neural network on the carla simulator," in *Conference on IEEE Intelligent Vehicles Symposium*, 2024.

[20] H. Du and C.-M. Chew, "Transparking: A dual-decoder transformer framework with soft localization for end-to-end automatic parking," *arXiv preprint arXiv:2503.06071*, 2025.

[21] M. Tancik, P. Srinivasan, B. Mildenhall, S. Fridovich-Keil, N. Raghavan, U. Singhal, R. Ramamoorthi, J. Barron, and R. Ng, "Fourier features let networks learn high frequency functions in low dimensional domains," *Advances in neural information processing systems*, vol. 33, pp. 7537–7547, 2020.

[22] N. Rahaman, A. Baratin, D. Arpit, F. Draxler, M. Lin, F. Hamprecht, Y. Bengio, and A. Courville, "On the spectral bias of neural networks," in *Proceedings of the 36th International Conference on Machine Learning*, ser. Proceedings of Machine Learning Research, K. Chaudhuri and R. Salakhutdinov, Eds., vol. 97. PMLR, 09–15 Jun 2019, pp. 5301–5310. [Online]. Available: <https://proceedings.mlr.press/v97/rahaman19a.html>

[23] M. Bojarski, D. D. Testa, D. Dworakowski, B. Firner, B. Flepp, P. Goyal, L. D. Jackel, M. Monfort, U. Muller, J. Zhang, X. Zhang, J. Zhao, and K. Zieba, "End to end learning for self-driving cars," *CoRR*, vol. abs/1604.07316, 2016. [Online]. Available: <http://arxiv.org/abs/1604.07316>

[24] M. Bojarski, P. Yeres, A. Choromanska, K. Choromanski, B. Firner, L. Jackel, and U. Muller, "Explaining how a deep neural network trained with end-to-end learning steers a car," *arXiv preprint arXiv:1704.07911*, 2017.

[25] K. Chitta, A. Prakash, B. Jaeger, Z. Yu, K. Renz, and A. Geiger, "Transfuser: Imitation with transformer-based sensor fusion for autonomous driving," *Pattern Analysis and Machine Intelligence (PAMI)*, 2023.

- [26] K. Cho, B. van Merriënboer, D. Bahdanau, and Y. Bengio, “On the properties of neural machine translation: Encoder–decoder approaches,” in *Proceedings of SSTS-8, Eighth Workshop on Syntax, Semantics and Structure in Statistical Translation*, D. Wu, M. Carpuat, X. Carreras, and E. M. Vecchi, Eds. Doha, Qatar: Association for Computational Linguistics, Oct. 2014, pp. 103–111. [Online]. Available: <https://aclanthology.org/W14-4012/>
- [27] Y. Hu, J. Yang, L. Chen, K. Li, C. Sima, X. Zhu, S. Chai, S. Du, T. Lin, W. Wang, L. Lu, X. Jia, Q. Liu, J. Dai, Y. Qiao, and H. Li, “Planning-oriented autonomous driving,” in *Proceedings of the IEEE/CVF Conference on Computer Vision and Pattern Recognition*, 2023.
- [28] C. Li, Z. Ji, Z. Chen, T. Qin, and M. Yang, “Parkinge2e: Camera-based end-to-end parking network, from images to planning,” in *2024 IEEE/RSJ International Conference on Intelligent Robots and Systems (IROS)*, 2024, pp. 13206–13212.
- [29] A. Vaswani, N. Shazeer, N. Parmar, J. Uszkoreit, L. Jones, A. N. Gomez, L. Kaiser, and I. Polosukhin, “Attention is all you need,” in *Proceedings of the 31st International Conference on Neural Information Processing Systems*, ser. NIPS’17. Red Hook, NY, USA: Curran Associates Inc., 2017, pp. 6000–6010.
- [30] J. Wei, N. Vödisch, A. Rehr, C. Feist, and A. Valada, “Parkdiffusion: Heterogeneous multi-agent multi-modal trajectory prediction for automated parking using diffusion models,” *arXiv preprint arXiv:2505.00586*, 2025.
- [31] M. Jiang, Y. Li, S. Zhang, S. Chen, C. Wang, and M. Yang, “Hope: A reinforcement learning-based hybrid policy path planner for diverse parking scenarios,” *arXiv preprint arXiv:2405.20579*, 2024.
- [32] Y. Li, K. Xiong, X. Guo, F. Li, S. Yan, G. Xu, L. Zhou, L. Chen, H. Sun, B. Wang *et al.*, “Recogdrive: A reinforced cognitive framework for end-to-end autonomous driving,” *arXiv preprint arXiv:2506.08052*, 2025.
- [33] J. Chen, A. Shen, F. Wanghan, and C. Liang, “Quantitative analysis of parking difficulty via vehicle kinematics,” in *2024 8th CAA International Conference on Vehicular Control and Intelligence (CVCI)*, 2024, pp. 1–6.